JOURNAL OF SPACECRAFT AND ROCKETS
Vol. 31, No. 5, September–October 1994

Higher-Order Viscous Shock-Layer Solutions for High-Altitude Flows

Roop N. Gupta* and Ernest V. Zoby*
NASA Langley Research Center, Hampton, Virginia 23681-0001
and
Sudheer N. Nayani† and Kam-Pui Lee†
ViGYAN, Inc. Hampton, Virginia 23666

A higher-order viscous-shock-layer method has been developed and is used to obtain physically consistent results under varying degrees of low-density conditions for perfect-gas and nonequilibrium flows past slender bodies. The method of solution is a spatial-marching, implicit finite-difference technique, which employs a Vigneron pressure condition in the subsonic nose region. Higher-order body and shock slip conditions are employed with the method to obtain solutions for the low-density flows. Detailed comparisons with the direct simulation Monte Carlo method and Navier-Stokes calculations clearly show that the higher-order terms included in the HVSL equations are required to predict comparable values of surface pressure and heat transfer rate at higher altitude. The deficiency of the standard viscous shock-layer method in predicting low-density flows can not be corrected by the slip conditions alone as considered by earlier researchers.

Nomenclature

A^* = local cross-sectional area, ft^2
C_D = total drag coefficient based on the local cross-sectional area, 2 drag/$(\rho^*_\infty U^{*2}_\infty A^*)$
C_H = heat-transfer coefficient,$2q^*/(\rho^*_\infty U^{*3}_\infty)$
C_i = mass fraction of species i
C_p = pressure coefficient, $2p^*/(\rho^*_\infty U^{*2}_\infty)$
$\hat{C}_p$ = frozen specific heat of mixture, $\sum_i C_i C_{p,i}$
$C_{p,i}$ = specific heat of species i, $C^*_{p,i}/C^*_{p,\infty}$
$C^*_{p,\infty}$ = freestream specific heat, Btu/lbm·°R
D_{ij} = binary diffusion coefficients
g = stretching function
H = total enthalpy, $h + u^2/2$
h = enthalpy of mixture,$\sum_i C_i h_i$
h_1, h_3 = shape factors defined by Eq. (A12)
h_i = enthalpy of species i, h^*_i/U^{*2}_∞
K = thermal conductivity of mixture, $K^*/(\mu^*_{\text{ref}} C^*_{p,\infty})$
Kn = Knudsen number, λ^*/R^*_N
Le = binary Lewis number, $\rho^* D^*_{ij} \hat{C}^*_p/K^*$
M_∞ = freestream Mach number
M^*_i = molecular weight of species i, lbm/lb-mole
$\bar{M}^*$ = molecular weight of mixture, lbm/lb-mole
N_s = number of reacting species
n = coordinate measured normal to the body, n^*/R^*_N
p = Pressure, $p^*/(\rho^*_\infty U^{*2}_\infty)$
Pr = Prandtl number
q_w = wall heat-transfer rate, $q^*_w/(\rho^*_\infty U^{*3}_\infty)$
R^* = universal gas constant, 4.968×10^4 lbm · ft^2/s^2· lb-mole ·°R
R^*_N = nose radius, ft
Re_∞ = Reynolds number, $\rho^*_\infty U^*_\infty R^*_N/\mu^*_\infty$
r = radius of the body surface, r^*/R^*_N
s = coordinate measured along the body surface, s^*/R^*_N
T = temperature, T^*/T^*_{ref}
T_{ref} = $U^{*2}_\infty/C^*_{p,\infty}$, °R
U^*_∞ = freestream velocity, ft/s
u = velocity component tangent to body surface, u^*/U^*_∞
v = velocity component normal to body surface, v^*/U^*_∞
W = dummy variable used in Eq. (1)
$\dot{w}_i$ = mass rate of formation of species, i, $\dot{w}^*_i R^*_N/(\rho^*_\infty U^*_\infty)$
x_i = mole fraction of species i
α = shock angle defined in Fig. 2
$\alpha_1, \alpha_2, \alpha'_3, \alpha_3, \alpha_4$ = coefficient in Eq. (1)
β = angle defined in Fig. 2
Δh^{*f}_i = heat of formation of species i, Btu/lbm
ε = Reynolds-number parameter, $(\mu^*_{\text{ref}}/\rho^*_\infty U^*_\infty R^*_N)^{1/2}$
ξ = coordinate measured along the body surface, s
$\bar{\eta}$ = transformed n coordinate n/n_{sh}
η = transformed $\bar{\eta}$ coordinate, $g(\bar{\eta})$
θ = body angle defined in Fig. 2
κ = body curvature, $\kappa^* R^*_N$
λ^* = mean free path, ft
μ = mixture viscosity, μ^*/μ^*_{ref}
μ^*_{ref} = reference viscosity, $\mu^*(T^*_{\text{ref}})$, lbm/ft·s
ρ = density of mixture, ρ^*/ρ^*_∞

Subscripts

i = ith species
m = body station
max = maximum
ref = reference
sh = shock
w = wall
∞ = freestream

Presented as Paper 93-2724 at the AIAA 28th Thermophysics Conference, Orlando, FL, July 6–9, 1993; received July 13, 1993; revision received Jan. 25, 1994; accepted for publication Jan. 27, 1994. Copyright © 1994 by the American Institute of Aeronautics and Astronautics, Inc. No copyright is asserted in the United States under Title 17, U.S. Code. The U.S. Government has a royalty-free license to exercise all rights under the copyright claimed herein for Governmental purposes. All other rights are reserved by the copyright owner.

*Aero-Space Technologist, Aerothermodynamics Branch, Space Systems Division. Associate Fellow AIAA.
†Research Engineer. Member AIAA.

Superscripts

*	= dimensional quantity
~	= shock-oriented velocity components
-	= quantity divided by its correspoding shock value
/	= total differential with respect to ξ

Introduction

TRANSATMOSPHERIC vehicles (TAV), which employ air-breathing propulsion,[1] will traverse a large range of Reynolds numbers and Mach numbers during both ascent and descent. These vehicles are typically slender with small leading edges. While the high-Reynolds-number and high-Mach-number conditions at low altitudes are critical to the design process, the high-altitude (low-density) flight conditions can also be important.

The influence of low-density nonequilibrium chemistry on the slender-body aerodynamics and the aerothermal issues can be important for maneuvers or cruise at high altitudes. The small leading edges will experience large convective heating rates, and the reduction in the resulting high temperatures may be achieved by active cooling. The weight of the coolant required can be substantial and ultimately can result in lower payload weights. Therefore, the accurate prediction of the aerothermal conditions over the entire Reynolds-number range is obviously important. A perfect-gas viscous-shock-layer (VSL) analysis with shock and body slip was employed in Ref. 2 to investigate the low-density effects on slightly blunted slender bodies. An interesting result of this investigation was that the standard VSL equations[3] do not properly model the flowfield physics at lower densities even with surface and shock slip conditions. This problem has been attributed to the fact that the VSL equations do not contain the necessary viscous terms in the normal momentum equation. The trend of predicted stagnation-point pressure-coefficient values in comparison with the results obtained from a Navier-Stokes (NS) solution[2] was shown to be physically inconsistent at higher altitudes. The influence of a nonequilibrium chemistry assumption (for the flowfield chemistry) on the stagnation-point heating compared with an equilibrium air condition was presented in Ref. 4. This analysis, however, did not provide the nonequilibrium comparisons with slip condition at lower densities.

This investigation presents a solution of the modified VSL equations that retain additional higher-order terms (HOT) in the normal momentum and energy equations and provide physically consistent results similar to a NS calculation. These higher-order terms, although of a lower order of magnitude then the VSL terms, have been retained in order to increase the accuracy in the caculation of pressure and temperature through the layer at low densities (or Reynolds numbers). Further, these terms, even though not needed in a VSL analysis, are also retained for the purpose of extending the viscous-layer calculation to the merged-layer regime, where the shock thickness must be taken into consideration (either through the shock-slip relations or by integrating through the shock transition zone to freestream).

The advantage of employing the higher-order viscous-shock-layer (HVSL) equations is that significantly lower computer time and storage is required with these equations than with a NS solution. This improvement is very desirable in a conceptual or preliminary design process, where many trajectory points must be analyzed. The accuracy of the HVSL results is established by detailed comparisons with the NS calculations. Comparisons are also provided with the direct simulation Monte Carlo (DSMC) method and with the existing VSL method to note the current improvements for low-density flows.

Overview of the Flowfield Equations and Solution Method

Solution of the complete NS equations with wall slip conditions is required to obtain physically consistent results[5] from a continuum analysis under low-density (high-altitude) flight conditions. However, due to the large computer resource requirement for a full NS solution,[6] it is advantageous (also from a numerical point of view) to seek more efficient and equally accurate solutions. The "parabolized" form of these equations offers such an option, since the least-difficult partial differential equations to solve numerically (especially, for long slender bodies) are the parabolic ones. Therefore, as far as the numerical solutions are concerned, once the equations are made parabolic or quasi-parabolic, there is no numerical advantage to further simplification. The parabolic partial differential equations can be solved very efficiently by a spacemarching method with much less computer resources (both storage and time) than for typical NS solvers, which are basically elliptic in character.

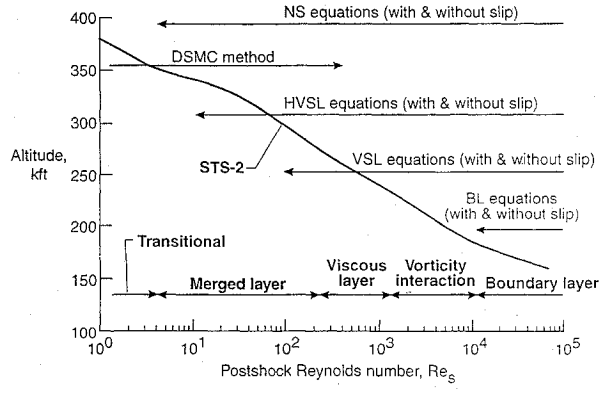

Fig. 1 Flow regimes and flowfield equations versus stagnation postshock Reynolds number.

The HVSL equations employed in this study are a parabolized form of the NS equations. For an axisymmetric body at 0-deg angle of attack, they are similar to the parabolized Navier-Stokes (PNS) equations.[7] They fall between the NS and VSL equations and differ from the VSL equations in that they retain viscous diffusion and curvature terms in the normal momentum equation. Figure 1 illustrates the limits of applications of the various flowfield equations in different flow regimes. This classification is based on stagnation-point heating comparisons with flight data and is adapted from Probstein.[8]

The HVSL equations do not require a starting solution, but need an input shock shape similar to the VSL equations.[9] Further, they are self-starting and provide a solution over the subsonic nose region through a globally iterative procedure (similar to the one used for the VSL equations). The HVSL (as well as the VSL) solutions presented here are obtained with high-order surface boundary conditions, which become important at higher altitude. These high-order boundary conditions were not included in the results of Ref. 2.

Analysis

Governing Equations

The conservation equations employed in this analysis are the steady, perfect-gas, and nonequilibrium form of the HVSL equations for an axisymmetric body at 0-deg angle of attack (see Fig. 2). These equations in the orthogonal, body-oriented transformed coordinates and normalized form are given here. The second-order partial differential equations are written in the form

$$\frac{\partial^2 W}{\partial \eta^2} + \frac{(\mathrm{d}^2 g/\mathrm{d}\bar{\eta}^2) + \alpha_1(\mathrm{d}g/\mathrm{d}\bar{\eta})}{(\mathrm{d}g/\mathrm{d}\bar{\eta})^2}\frac{\partial W}{\partial \eta} + \frac{\alpha_2}{(\mathrm{d}g/\mathrm{d}\bar{\eta})^2}W + \frac{\alpha_3 + \alpha_3'}{(\mathrm{d}g/\mathrm{d}\bar{\eta})^2} + \frac{\alpha_4}{(\mathrm{d}g/\mathrm{d}\bar{\eta})^2}\frac{\partial W}{\partial \xi} = 0 \qquad (1)$$

where $\mathrm{d}g/\mathrm{d}\bar{\eta}$ and $\mathrm{d}^2 g/\mathrm{d}\bar{\eta}^2$ are the first and second derivatives of the stretching function $g(\bar{\eta})$ given in Ref. 9. The quantity W represents $\bar{u}$ in the s-momentum equation and $\bar{T}$ and $\bar{H}$ in the energy equation for nonequilibrium and perfect gas, respectively. The coefficients α_1 to α_4 are given in the Appendix. The remaining equations are written in the following form:

1) Global continuity:

$$\frac{\partial}{\partial \xi}\left[n_{sh}h_3\rho_{sh}u_{sh}\frac{\bar{M}_\infty^*}{\bar{M}_{sh}^*}\frac{\bar{p}\bar{u}}{\bar{T}}\right] + \left(\frac{\mathrm{d}g}{\mathrm{d}\eta}\right)\frac{\partial}{\partial \eta}\left\{h_3\left[h_1\rho_{sh}\frac{\bar{M}_\infty^*}{\bar{M}_{sh}^*}\frac{\bar{p}v}{\bar{T}} - \bar{\eta}n_{sh}'\rho_{sh}u_{sh}\frac{\bar{M}_\infty^*}{\bar{M}_{sh}^*}\frac{\bar{p}\bar{u}}{\bar{T}}\right]\right\} = 0 \qquad (2)$$

2) n-Momentum:

$$\frac{u_{sh}n_{sh}\bar{p}\bar{u}}{h_1}\frac{\partial v}{\partial \xi} - \frac{u_{sh}n'_{sh}\bar{\eta}\bar{u}\bar{p}}{h_1}\frac{\partial v}{\partial \eta}\frac{dg}{d\bar{\eta}} + v\bar{p}\frac{\partial v}{\partial \eta}\frac{dg}{d\bar{\eta}} - \frac{n_{sh}u_{sh}^2\kappa\bar{u}^2\bar{p}}{h_1} + \left(\frac{R^*}{\bar{M}^*C^*_{p,\infty}}\right)T_{sh}\bar{T}\frac{\partial \bar{p}}{\partial \eta}\frac{dg}{d\bar{\eta}} = \frac{n_{sh}T_{sh}}{p_{sh}}\bar{T}\left(\frac{R^*}{\bar{M}^*C^*_{p,\infty}}\right) \times \text{HOT} \tag{3}$$

where

$$\text{HOT} = \frac{4}{3}\varepsilon^2\frac{\mu_{sh}}{n_{sh}}\left[\frac{\bar{\mu}}{n_{sh}}\left\{\frac{\partial^2 v}{\partial \eta^2}\left(\frac{dg}{d\bar{\eta}}\right)^2 + \frac{\partial v}{\partial \eta}\frac{d^2 g}{d\bar{\eta}^2}\right\} + \frac{1}{n_{sh}}\frac{\partial \bar{\mu}}{\partial \eta}\frac{\partial v}{\partial \eta}\left(\frac{dg}{d\bar{\eta}}\right)^2 + \left(\bar{\mu}\frac{\partial v}{\partial \eta} - \frac{1}{2}v\frac{\partial \bar{\mu}}{\partial \eta}\right) \times \left(\frac{dg}{d\bar{\eta}}\right)\left(\frac{\kappa}{h_1} + \frac{\cos\theta}{h_3}\right) - n_{sh}\bar{\mu}v\left(\frac{\kappa^2}{h_1^2} + \frac{\cos^2\theta}{h_3^2}\right)\right] \tag{4}$$

3) Equation of state:

$$\bar{p} = \bar{\rho}\bar{T}\left(\bar{M}^*_{sh}/\bar{M}^*\right) \tag{5}$$

Since the global continuity equation (2) and the normal momentum equation (3) are solved in a coupled way for $\bar{p}$ and v, Eq. (3) is reduced to a first-order equation in v by eliminating $\partial^2 v/\partial \eta^2$ in the higher-order terms (HOT) through the derivative of continuity equation:

$$\frac{\partial^2 v}{\partial \eta^2} = \frac{1}{(dg/d\eta)^2}\left(-\frac{\partial v}{\partial \eta}\frac{d^2 g}{d\eta^2} + \left[n_{sh}\frac{\partial}{\partial \xi}\left(h_3\frac{\bar{M}^*}{\bar{M}^*_{sh}}\rho_{sh}u_{sh}\frac{\bar{p}}{\bar{T}}\bar{u}\right) - n'_{sh}\bar{\eta}\frac{dg}{d\bar{\eta}}\frac{\partial}{\partial \eta}\left(h_3\frac{\bar{M}^*}{\bar{M}^*_{sh}}\rho_{sh}u_{sh}\frac{\bar{p}}{\bar{T}}\bar{u}\right) + v\frac{dg}{d\bar{\eta}}\frac{\partial}{\partial \eta}\left(h_1h_3\frac{\bar{M}^*}{\bar{M}^*_{sh}}\rho_{sh}\frac{\bar{p}}{\bar{T}}\right)\right] \times \left[\frac{1}{h_1h_3}\left(\frac{\bar{M}^*_{sh}}{\bar{M}^*}\right)^2\frac{1}{\rho_{sh}}\left(\frac{\bar{T}}{\bar{p}}\right)^2\frac{dg}{d\bar{\eta}}\frac{\partial}{\partial \eta}\left(\frac{\bar{M}^*}{\bar{M}^*_{sh}}\frac{\bar{p}}{\bar{T}}\right) + \left(\frac{\bar{M}^*_{sh}}{\bar{M}^*}\right)\frac{1}{\rho_{sh}}\frac{1}{(h_1h_3)^2}\frac{\bar{T}}{\bar{p}}\frac{dg}{d\bar{\eta}}\frac{\partial}{\partial \eta}(h_1h_3)\right] - \left[\left(\frac{\bar{M}^*_{sh}}{\bar{M}^*}\right)\frac{1}{\rho_{sh}}\frac{1}{h_1h_3}\frac{\bar{T}}{\bar{p}}\right] \times \left\{n_{sh}\frac{dg}{d\bar{\eta}}\frac{\partial^2}{\partial \eta \partial \xi}\left(h_3\frac{\bar{M}^*}{\bar{M}^*_{sh}}\rho_{sh}u_{sh}\frac{\bar{P}}{\bar{T}}\bar{u}\right) - n'_{sh}\bar{\eta}\left(\frac{dg}{d\bar{\eta}}\right)\frac{\partial}{\partial \eta}\left[\frac{dg}{d\bar{\eta}}\frac{\partial}{\partial \eta}\left(h_3\frac{\bar{M}^*}{\bar{M}^*_{sh}}\rho_{sh}u_{sh}\frac{\bar{P}}{\bar{T}}\bar{u}\right)\right] - n'_{sh}\frac{dg}{d\bar{\eta}}\frac{\partial}{\partial \eta}\left(h_3\frac{\bar{M}^*}{\bar{M}^*_{sh}}\rho_{sh}u_{sh}\frac{\bar{P}}{\bar{T}}\bar{u}\right) + \left(\frac{dg}{d\bar{\eta}}\right)^2\frac{\partial v}{\partial \eta}\frac{\partial}{\partial \eta}\left(h_1h_3\frac{\bar{M}^*}{\bar{M}^*_{sh}}\rho_{sh}\frac{\bar{p}}{\bar{T}}\right) + v\frac{dg}{d\bar{\eta}}\frac{\partial}{\partial \eta}\left[\frac{dg}{d\bar{\eta}}\frac{\partial}{\partial \eta}\left(h_1h_3\frac{\bar{M}^*}{\bar{M}^*_{sh}}\rho_{sh}\frac{\bar{p}}{\bar{T}}\right)\right]\right\}\right) \tag{6}$$

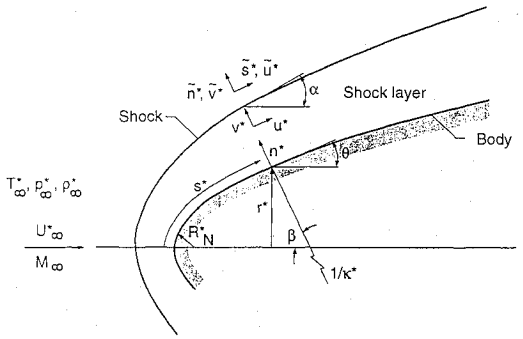

Fig. 2 Coordinate system.

For perfect-gas flow, the species continuity equation is not needed, and Eqs. (1–6) can be used for such a flow with the assumption

$$\frac{\bar{M}^*_{sh}}{\bar{M}^*_{\infty}} = 1 \tag{7}$$

Boundary Conditions

The wall boundary conditions are those of Ref. 10. The slip conditions for velocity, temperature, pressure, and species concentration in a body-oriented coordinate system (used here) for two-dimensional (2D) flows are provided in Appendix D of Ref. 10. These may also be obtained from the 3D boundary conditions given in body-oriented coordinates in Ref. 11.

The transformed shock conditions employed are

$$\bar{u} = \bar{T} = \bar{H} = \bar{\rho} = \bar{p} = 1 \tag{8}$$

and

$$v_{sh} = u_{sh}\tan(\alpha - \theta) - \frac{\sin\alpha}{\rho_{sh}\cos(\alpha - \theta)} \tag{9}$$

at $\eta = 1$. Note that for nonequilibrium flow, the species mass fractions and the normal velocity are not normalized with their respective shock values. The nondimensional form of the normal velocity is solved for the perfect-gas case also.

The shock conditions in the nondimensional form are given in Appendix B of Ref. 12. These may also be obtained from those given in Ref. 11 for the 3D flows.

The shock slip conditions are the modified Rankine-Hugoniot relations, which are obtained from the integration of one-dimensional NS equations through the shock transition zone. The integration is carried out from the interface behind the shock transition zone (where the usual Rankine-Hugoniot shock relations apply) to freestream. Cheng[13] first provided these shock-slip relations for the stagnation region, and they were subsequently used by Blottner et. al.[14] for a similar analysis. These relations are also applicable for a curvilinear shock if the shock thickness is much less than the radius of curvature of the shock.[15] The present shock-slip equations can be employed for both stagnation-point and downstream shock-layer analysis with a similar shock-thickness limitation.

Chemical Kinetics, Thermodynamic, and Transport Properties

The details of the nonionized five-species (O, N, O_2, N_2, and NO) air chemical kinetics, thermodynamic, and transport properties employed in this study are given in Ref. 16. A variable Prandtl number has been used in this study. The mixture viscosity is obtained by using the Wilke relation (from Ref. 16), and the mixture thermal conductivity is calculated using the formula of Mason and Saxena.[17] A constant value of 1.4 is employed for the Lewis number Le.

Method of Solution

The method used for solving the HVSL equations with slip conditions is essentially the same as that described in Refs. 2 and 18. This method is a spatial-marching, implicit, finite-difference technique, which includes coupling of the global continuity and normal momentum equations and use of the Vigneron pressure condition[9]

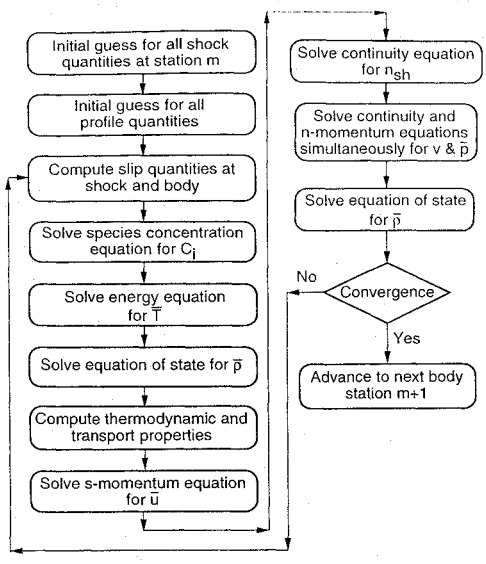

Fig. 3 Solution sequence with shock and body slip for nonequilibrium flow chemistry (at body station *m*).

in the subsonic nose region. The second derivative of the normal velocity $\partial^2 v/\partial\eta^2$ appearing in the HOT of the normal momentum equation. (3) is eliminated through Eq. (6). The first derivative of v (i.e., $\partial v/\partial\eta$) appearing in the higher-order terms is then combined with the corresponding derivative terms on the left-hand side of Eq. (3). Equations (2) and (3) are now solved simultaneously through a coupled procedure[9,18] with the remainder of the HOT lagging by a global pass. Figure 3 shows the solution sequence for obtaining the nonequilibrium HVSL solutions with body and shock slip at a given body station m. A similar sequence is employed for the perfect-gas solutions except that no species concentration equations are to be solved and the energy equation is solved in terms of $\bar{H}$ (in place of $\bar{T}$).

Similar to the approaches of Refs. 5, 9, and 18, the stagnation-point solution for the HVSL equations is obtained by expanding the various flowfield quantities in terms of the distance ξ along the body surface. These series expansions reduce the partial differential equations (1–3) to ordinary differential equations in terms of η. These equations are then integrated normal to the surface with appropriate shock and body slip conditions. The solution procedure[5,9,18] marches along the body beyond stagnation point using Eqs. (1–3).

The solution procedure for the HVSL equations is found computationally more efficient and stable if the coupling between the normal momentum and global continuity equations is implemented through an iterative procedure (rather than a simultaneous solution) over the subsonic nose region with the Vigneron condition. The simultaneous solution of the two equations is usually required beyond the subsonic nose region, where the normal velocity becomes small for slender bodies.

Results and Discussion

Numerical solutions of the HVSL equations for the low-density, perfect-gas, nonequilibrium hypersonic flow over long slender bodies with small leading edges are obtained. The higher-order surface and shock slip boundary conditions are implemented in an implicit finite-difference method used to solve the governing equations. Detailed comparisons with other predictions and experimental data for the low-density hypersonic conditions are included for several conditions. Results are also presented for the low-density segment of an assumed entry trajectory considered earlier.[1,4]

Comparisons with Other Prediction Methods

Perfect-Gas Comparisons

A comparison of the HVSL results with those obtained from the Langley Aerothermodynamic Upwind Relaxation Algorithm[6] (LAURA) and VSL equations[9,18] is provided in Ref. 12. The predictions are in quite good agreement. Both of these prediction methods include similar higher-order terms in the normal momentum equations as compared to those in the VSL method. These results also quantify the role played by the higher-order terms under the low-density flow conditions. The low-density effects are characterized by the Reynolds- number parameter $^{2,3}\varepsilon$ and become generally significant[12] for values of ε greater than 0.1.

The pressure and heat-transfer coefficients at different altitudes are shown in Figs. 4a and 4b, respectively. The VSL and NS calculation results are similar to those of Ref. 2, except that the higher-order terms (see Appendix D of Ref. 10) omitted in the body slip equations of Ref. 2 are included in the present results. The inclusion of these terms does improve the trend of the pressure coefficient at higher altitudes (compare the VSL predictions in Fig. 4a with those given in Fig. 6a of Ref. 2). These values are still lower than the NS calculations. Clearly, the higher-order terms included in the HVSL equations are required to predict values comparable to the NS results. Also, the VSL calculations with the body-slip constants of Ref. 19 give values of C_p which are considerably greater than the NS calculated values (Fig. 4a). Further, the trend of C_p values predicted with the slip constants of Ref. 19 is quite different from that of the NS (or HVSL) calculations with increasing altitude (or decreasing density). It should be mentioned here that the body-slip constants were modified in Ref. 19 to match the predicted wall pressure distribution to experimental data. Obviously, as may be noticed from Fig. 4a, the arbitrary values assigned in Ref. 19 to the body slip constants are not applicable for the present comparisons. The trend of the C_p values with decreasing density as predicted by the NS calculations in Fig. 4a is similar to that of the NS predictions of Ref. 20, which compared C_p values with the data of Ref. 21. The VSL calculations (with the present body and shock slip conditions as well as with the body slip conditions proposed in Ref. 19) pre-

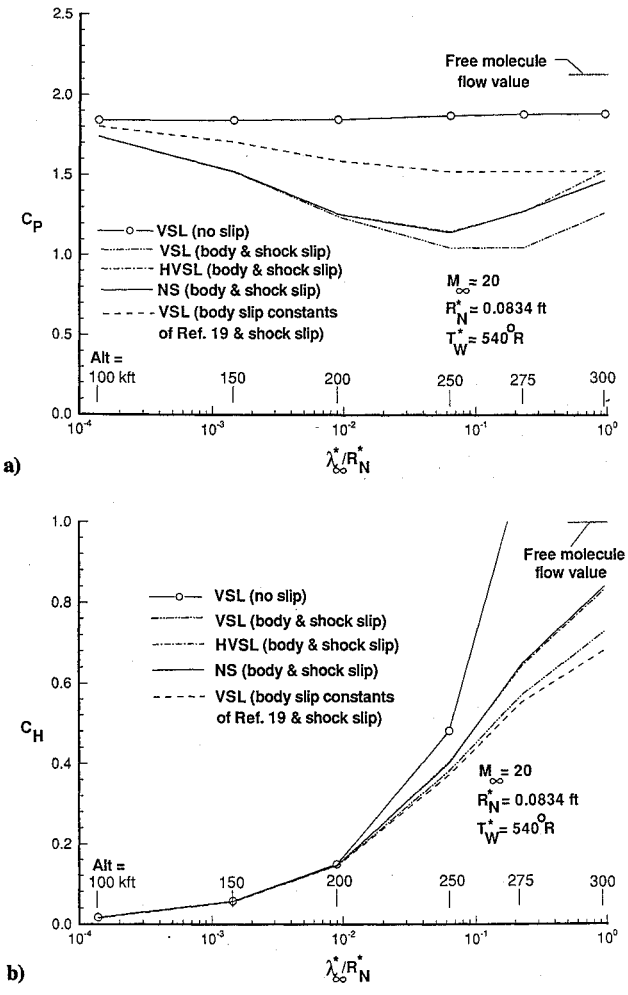

Fig. 4 a) Stagnation-point values of pressure coefficient versus Knudsen number and b) stagnation point values of heat-transfer coefficient versus Knudsen number.

Table 1 Flowfield conditions[a] and stagnation-point perfect-gas heat-transfer values

Case	p^*_∞, atm	T^*_∞, °R	ρ^*_∞, lbm/ft^3	U^*_∞, ft/s	M_∞	Kn_∞	q^*_w, Btu/ft^2-s HVSL[b]	q^*_w, Btu/ft^2-s DSMC
1 (Ref. 2)	0.2008×10^{-4}	352.0	0.2263×10^{-5}	18,394	20.0	0.0632	113.20	118.15
2 (Ref. 23)	0.2076×10^{-4}	27.0	2.9123×10^{-5}	5,358	20.6	0.0012	9.30	8.50

[a] $R^*_N = 0.833 \times 10^{-1}$ ft (Case 1), $R^*_N = 0.4095 \times 10^{-1}$ ft (case 2), $T^*_W = 540°R$ (cases 1, 2)
[b] With shock and body slip.

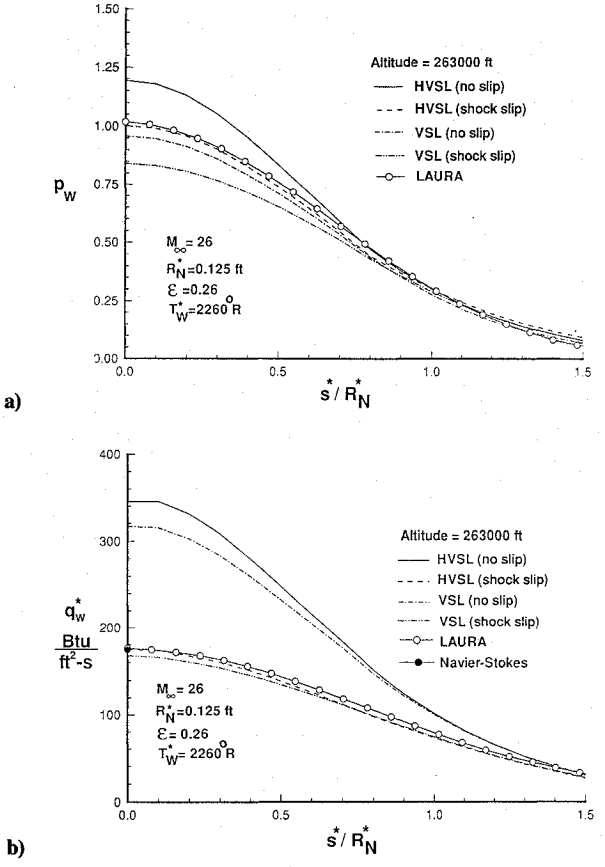

Fig. 5 Comparison of a) predicted surface pressure for nonequilibrium flow over a fully catalytic sphere and b) predicted surface heat transfer rate for nonequilibrium flow over a fully catalytic sphere.

dict lower values of the heat-transfer coefficient than the NS and HVSL calculations shown in Fig. 4b. Figures 4a and 4b highlight the role played by the higher-order terms for high-altitude (or low-Reynolds-number) flows. At lower altitudes (or higher values of the Reynolds-number), the HVSL (and NS) predictions reduce to those obtained by the VSL calculations as expected, and the higher-order terms give a negligible contribution.

Some perfect-gas comparisons of the HVSL results with the direct simulation Monte Carlo (DSMC) method[22] are shown in Table 1. Both of the calculations shown in this table are in the continuum regime ($Kn_\infty < 0.1$). It is therefore believed that the HVSL heat-transfer results are quite accurate for these two cases. The difference between the HVSL and DSMC calculations is less than 5% for case 1 and less than 9% for case 2.

Nonequilibrium Flow Comparisons

Comparisons of results for nonequilibrium flow are shown in Figs. 5 and 6. Both surface pressure and heat transfer results are predicted to be the same from the HVSL (with shock slip) and LAURA calculations. The VSL (with shock slip) results are once again lower, due to the omission of high-order terms in the normal momentum equation. Figures 5b and 6 also contain results from the stagnation-region NS code.[5] The NS method captures the shock as part of the solution process, and hence shock slip is implicitly accounted for in the results.

Table 2 Freestream condition and other parameters[a] for an assumed entry trajectory

Time, s	Altitude, ft	Density, lbm/ft^3	$U^*_{\infty'}$ ft/s	$T^*_{\infty'}$ °R	ε or $1/\sqrt{Re}_{ref}$	Kn^b_∞	M_∞
1140	290720	0.2727×10^{-6}	24180	336	0.525	0.3449	27.03
1200	263000	0.1113×10^{-5}	24200	358	0.260	0.0857	26.13
1330	225000	0.6167×10^{-5}	24020	402	0.110	0.0158	24.46
1440	225000	0.6167×10^{-5}	23740	402	0.110	0.0158	24.17
1680	225390	0.6193×10^{-5}	23110	402	0.110	0.0158	23.51
1980	226000	0.6029×10^{-5}	22350	400	0.111	0.0162	22.79
2280	211000	0.1102×10^{-4}	21330	420	0.082	0.0089	21.16
2640	198500	0.1813×10^{-4}	19490	440	0.064	0.0055	18.91
2820	190000	0.2504×10^{-4}	18270	455	0.054	0.0040	17.47
3000	183500	0.3173×10^{-4}	16760	465	0.048	0.0032	15.86
3360	160600	0.7297×10^{-4}	13910	487	0.032	0.0014	11.93

[a] $R^*_N = 0.125$ ft, $\bar{M}^*_\infty = 28.862$ lb/lb-mole, $T^*_w = 2260°$ R, $x_{N_2} = 0.789$, $x_{O_2} = 0.211$.
[b] $Kn_\infty = \lambda^*_\infty / R^*_N$; $\lambda^*_\infty = (T^*_\infty / T^*_{ref})^\omega / [(2-\omega)^\omega \Gamma(2-\omega)\sqrt{2} n^* \sigma^*_{ref}]$;
$T^*_{ref} = 5184°$R, $d^*_{ref} = 1.011 \times 10^{-9}$ ft (for N_2), $\sigma^*_{ref} = \pi d^{*2}_{ref}$, $s = 0.73$, $\omega = s - \frac{1}{2}$.

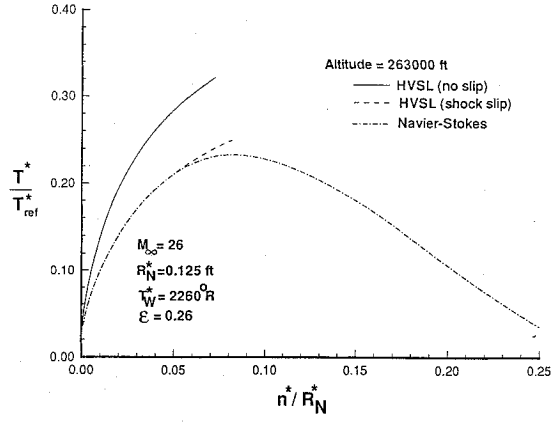

Fig. 6 Comparison of stagnation streamline temperature profiles for a fully catalytic surface.

As expected, the HVSL (with shock slip), LAURA, and NS code of Ref. 5 give almost the same stagnation-point heat-transfer values as shown in Fig. 5b. All the three methods contain similar significant higher-order terms in the normal momentum equation. The influence of the shock slip boundary condition on the flowfield structure is highlighted with the stagnation-temperature profile shown in Fig. 6. The importance of shock slip is clearly shown in this figure. The HVSL method computes to a shock boundary, whereas the NS method[5] integrates to the freestream.

Stagnation-Point Heating Rates and Pressure Coefficients for an Entry Trajectory

For an assumed entry (see Table 2) similar to that presented in Refs. 1 and 4, the predicted stagnation-point heating-rate histories are presented in Figs. 7a and 7b from the VSL and HVSL methods, respectively. These calculations are for nonequilibrium flow with three different surface conditions, a nose radius of 0.125 ft, and a wall temperature of 2260°R. In both Figs. 7a and 7b, the slip (or low-density) effects (which produce lower heating) are present in the trajectory prior to a time of 3000 s (or altitudes greater than about 183,500 ft). These slip effects are maximum for a noncatalytic wall (NCW) and minimum for a fully catalytic one (FCW).

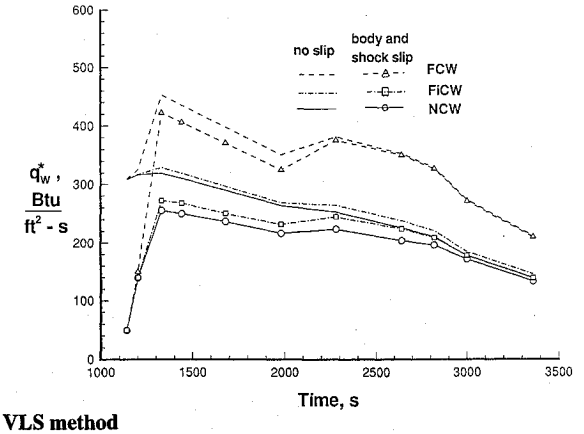

a) VLS method

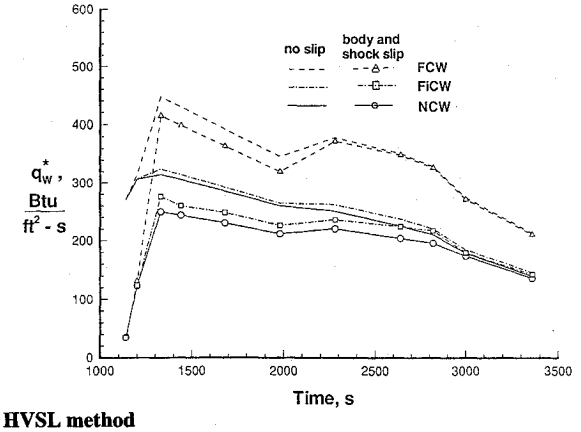

b) HVSL method

Fig. 7 Predicted time histories of the stagnation-point heating rate with different surface boundry conditions for nonequilibrium flow.

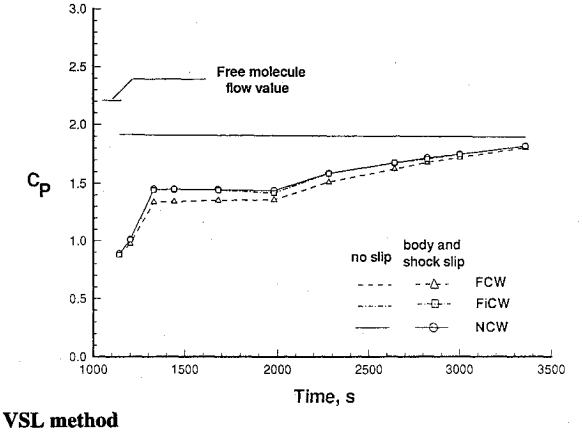

a) VSL method

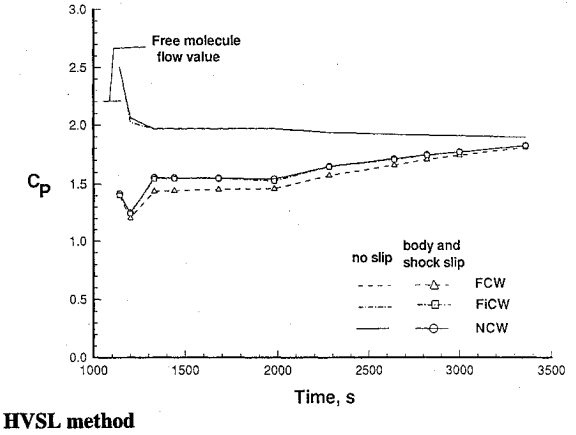

b) HVSL method

Fig. 8 Predicted time histories of the stagnation-point pressure coefficient for different surface boundary conditions for nonequilibrium flow.

As demonstrated through the results presented earlier, the HVSL method provides the correct trend for various flowfield and surface quantities with low density effects. For the trajectory heating calculations shown in Figs. 7a and 7b, the differences between the HVSL and VSL methods may be noticed for times prior to 1300 s (or altitudes greater than about 225,000 ft). Also, the reasons for including slip in the calculations are compelling for design considerations. In Figs. 7a and 7b, the inclusion of slip effects results in a heating reduction of 10% or more at altitudes as low as 190,000 ft (or time 2820 s). These results, if applied to a transatmospheric vehicle (whose design may contain many linear feet of leading edges), suggest significantly less total heating and correspondingly lower cooling requirements. This saving in cooling requirement could translate to larger payload capability. Note here that a smaller nose radius would show even larger influence of slip effects than shown in Figs. 7a and 7b, and that would persist to altitudes lower (or times greater) than those shown in Figs. 7a and 7b.

For the pressure-coefficient calculations, the VSL predictions (Fig. 8a) continuously decrease with increasing altitude as noted earlier, whereas the HVSL predictions (Fig. 8b) increase at higher altitudes and tend towards the free-molecular-flow value, as seen in earlier calculations also.

Conclusions

The investigation demonstrates the ability of higher-order viscous-shock-layer (HVSL) method to analyze low-density perfect-gas and nonequilibrium flows past slender bodies. With the use of higher-order body and shock slip boundary conditions, the HVSL equations provide physically consistent results similar to a Navier-Stokes (NS) calculation, but with significantly less computational time and storage requirement. Extensive comparisons of the HVSL results with those obtained from the direct simulation Monte Carlo (DSMC) method, Langley Aerothermodynamic Upwind Relaxation Algorithm (LAURA) code, and a stagnation-region NS code are included under varying degrees of low-density flow conditions. The high-order body and shock slip conditions are also implemented with the viscous-shock-layer (VSL) equations. Even though the higher-order body-slip equations improve on earlier VSL predictions, the VSL equations still fail to give physically consistent results (especially, for the pressure coefficient) under fairly low-density conditions. As demonstrated through comparisons with the HVSL and NS results, reason for the failure of the VSL method at low density lies in the omission of higher-order terms in the governing equations, and not in the slip boundary conditions as claimed by earlier researchers. The inclusion of slip effects gives a significant heating and drag reduction below the no-slip results and could be very beneficial from a design perspective.

Appendix: Coefficients for the Second-Order Equations

For the steady-state HVSL equations for perfect-gas and nonequilibrium flow, the coefficients α_1, α_2, α_3, α_3', and α_4 appearing in Eq. (1) are defined as follows:

1) s-Momentum (perfect gas and nonequilibrium flow), $W = \bar{u}$:

$$\alpha_1 = \frac{1}{\mu}\frac{\partial \bar{\mu}}{\partial \eta}\frac{dg}{d\bar{\eta}} + \frac{n_{sh}\kappa}{h_1} + \frac{n_{sh}\cos\theta}{h_3} - \frac{\rho_{sh}n_{sh}\bar{\rho}v}{\varepsilon^2\mu_{sh}\bar{\mu}} + \frac{\rho_{sh}n_{sh}n'_{sh}u_{sh}}{\varepsilon^2\mu_{sh}h_1}\frac{\bar{\eta}\bar{\rho}\bar{u}}{\bar{\mu}} \tag{A1}$$

$$\alpha_2 = -\frac{n_{sh}\kappa}{h_1\bar{\mu}}\frac{\partial \mu}{\partial \bar{\eta}}\frac{dg}{d\bar{\eta}} - \frac{n_{sh}^2\kappa}{h_1}\left[\frac{\kappa}{h_1} + \frac{\cos\theta}{h_3}\right] - \frac{\rho_{sh}n_{sh}^2\kappa}{\varepsilon^2\mu_{sh}h_1}\frac{\bar{\rho}v}{\bar{\mu}} - \frac{\rho_{sh}n_{sh}^2u'_{sh}}{\varepsilon^2\mu_{sh}h_1}\frac{\bar{\rho}\bar{u}}{\bar{\mu}} \tag{A2}$$

$$\alpha_3 = -\frac{p_{sh}n_{sh}^2}{\varepsilon^2\mu_{sh}u_{sh}h_1\bar{\mu}}\left(\frac{\partial \bar{p}}{\partial \xi} + \frac{\bar{p}}{p_{sh}}\frac{dp_{sh}}{d\xi} - \frac{\bar{\eta}n'_{sh}}{n_{sh}}\frac{\partial \bar{p}}{\partial \eta}\frac{dg}{d\bar{\eta}}\right) \tag{A3}$$

$$\alpha_4 = -\frac{\rho_{sh}n_{sh}^2u_{sh}}{\varepsilon^2\mu_{sh}h_1}\frac{\bar{\rho}\bar{u}}{\bar{\mu}} \tag{A4}$$

2) Energy (perfect-gas flow), $W = H$:

$$\alpha_1 = \frac{1}{\bar{\mu}}\frac{\partial \bar{\mu}}{\partial \eta}\frac{\mathrm{d}g}{\mathrm{d}\bar{\eta}} + \left(\frac{n_{sh}\kappa}{h_1} + \frac{n_{sh}\cos\theta}{h_3}\right) + \frac{\rho_{sh}n_{sh}Pr}{\varepsilon^2\mu_{sh}\bar{\mu}} \times \left(\frac{u_{sh}n'_{sh}}{h_1}\bar{\rho}\bar{u}\bar{\eta} - \bar{p}v\right) \tag{A5}$$

$$\alpha_2 = -\frac{\rho_{sh}u_{sh}n^2_{sh}Pr}{\varepsilon^2\mu_{sh}h_1\bar{\mu}}\frac{H'_{sh}}{H_{sh}}\bar{\rho}\bar{u} \tag{A6}$$

$$\alpha_3 = \frac{Pr}{\bar{\mu}}\frac{n^2_{sh}}{H_{sh}\mu_{sh}}\left[\frac{1}{n_{sh}}\frac{\partial\phi}{\partial\eta}\frac{\mathrm{d}g}{\mathrm{d}\bar{\eta}} + \left(\frac{\kappa}{h_1} + \frac{\cos\theta}{h_3}\right)\phi\right] + \frac{Prn_{sh}v}{\varepsilon^2\mu_{sh}H_{sh}\bar{\mu}}\left(p_{sh}\frac{\partial\bar{p}}{\partial\eta}\left(\frac{\mathrm{d}g}{\mathrm{d}\bar{\eta}}\right) - \frac{n_{sh}\rho_{sh}u^2_{sh}\kappa}{h_1}\bar{\rho}\bar{u}^2\right) \tag{A7}$$

$$\alpha'_3 = \frac{\mathrm{HOT}}{\left(\varepsilon^2\mu_{sh}H_{sh}\bar{\mu}/Prn^2_{sh}\right)} \tag{A8}$$

$$\alpha_4 = -\frac{n^2_{sh}\rho_{sh}u_{sh}Pr}{\varepsilon^2\mu_{sh}h_1\bar{\mu}}\bar{\rho}\bar{u} \tag{A9}$$

where

$$\phi = u^2_{sh}\bar{u}\left[\frac{Pr-1}{Pr}\frac{\mu_{sh}\bar{\mu}}{n_{sh}}\frac{\partial\bar{\mu}}{\partial\eta}\frac{\mathrm{d}g}{\mathrm{d}\bar{\eta}} - \frac{\kappa\mu_{sh}}{h_1}\bar{\mu}\bar{u}\right] \tag{A10}$$

$$\mathrm{HOT} = 2\frac{\varepsilon^2\bar{\mu}\mu_{sh}}{n^2_{sh}}\left(\frac{\partial v}{\partial\eta}\right)^2\left(\frac{\mathrm{d}g}{\mathrm{d}\bar{\eta}}\right)^2 + 2\varepsilon^2\mu_{sh}\bar{\mu}\left(\frac{v^2\kappa^2}{h^2_1} + \frac{(v\cos\theta)^2}{h^2_3}\right) - \frac{2}{3}\varepsilon^2\frac{\mu_{sh}\bar{\mu}}{n^2_{sh}}\left(\frac{\mathrm{d}g}{\mathrm{d}\bar{\eta}}\right)^2\left(\frac{\partial v}{\partial\eta}\right)^2 - \frac{2}{3}\varepsilon^2\mu_{sh}\bar{\mu} \times\left(\frac{v^2\kappa}{h^2_1h_3n_{sh}}\frac{\mathrm{d}g}{\mathrm{d}\bar{\eta}}\frac{\partial}{\partial\eta}(h_1h_3) + \frac{v^2\cos\theta}{h_1h^2_3n_{sh}}\frac{\mathrm{d}g}{\mathrm{d}\bar{\eta}}\frac{\partial}{\partial\eta}(h_1h_3)\right) \tag{A11}$$

and

$$h_1 = 1 + n_{sh}\bar{\eta}\kappa$$

$$h_3 = r + \bar{\eta}n_{sh}\cos\theta \tag{A12}$$

3) Energy (nonequilibrium flow), $W = \bar{T}$:

$$\alpha_1 = \frac{1}{\bar{K}}\frac{\partial\bar{K}}{\partial\eta}\frac{\mathrm{d}g}{\mathrm{d}\bar{\eta}} + n_{sh}\left(\frac{\kappa}{h_1} + \frac{\cos\theta}{h_3}\right) + \frac{Le\ Pr_{sh}}{Pr}\frac{\bar{\mu}}{\bar{K}}\sum_{i=1}^{N_s}\frac{\partial C_i}{\partial\eta}\frac{\mathrm{d}g}{\mathrm{d}\bar{\eta}}\bar{C}_{p,i} - \frac{\rho_{sh}\hat{C}_{p,sh}n_{sh}}{\varepsilon^2K_{sh}\bar{K}}\bar{\rho}\bar{C}_p\left(v - \frac{u_{sh}n'_{sh}\bar{u}\bar{\eta}}{h_1}\right) \tag{A13}$$

$$\alpha_2 = -\frac{n^2_{sh}\rho_{sh}\hat{C}_{p,sh}u_{sh}}{\varepsilon^2k_{sh}T_{sh}h_1}\frac{\bar{\rho}\bar{C}_p\bar{u}}{\bar{K}}\frac{\mathrm{d}T_{sh}}{\mathrm{d}\xi} - \frac{n^2_{sh}\dot{w}_{sh_2}}{\varepsilon^2K_{sh}\bar{K}}\bar{\dot{w}}_2 \tag{A14}$$

$$\alpha_3 = -\frac{n^2_{sh}\dot{w}_{sh1}\bar{\dot{w}}_1}{\varepsilon^2K_{sh}T_{sh}\bar{K}} + \frac{n^2_{sh}\mu_{sh}\bar{\mu}}{K_{sh}T_{sh}\bar{K}} \times\left(\frac{u_{sh}}{n_{sh}}\frac{\partial\bar{u}}{\partial\eta}\frac{\mathrm{d}g}{\mathrm{d}\bar{\eta}} - \frac{\kappa u_{sh}\bar{u}}{h_1}\right)^2 + \frac{n^2_{sh}u_{sh}p_{sh}\bar{u}}{\varepsilon^2K_{sh}T_{sh}\bar{K}h_1}\left(\frac{\partial\bar{p}}{\partial\xi} + \frac{\bar{p}}{p_{sh}}\frac{\mathrm{d}p_{sh}}{\mathrm{d}\xi} - \frac{n'_{sh}\bar{\eta}}{n_{sh}}\frac{\partial\bar{p}}{\partial\eta}\frac{\mathrm{d}g}{\mathrm{d}\bar{\eta}}\right) + \frac{n_{sh}p_{sh}v}{\varepsilon^2K_{sh}T_{sh}\bar{K}}\frac{\partial\bar{p}}{\partial\eta}\frac{\mathrm{d}g}{\mathrm{d}\bar{\eta}} \tag{A15}$$

$$\alpha'_3 = \frac{\mathrm{HOT}}{\varepsilon^2K_{sh}T_{sh}\bar{K}/n^2_{sh}} \tag{A16}$$

$$\alpha_4 = -\frac{n^2_{sh}\rho_{sh}\hat{C}_{p,sh}u_{sh}\bar{\rho}\bar{C}_p\bar{u}}{\varepsilon^2K_{sh}h_1\bar{K}} \tag{A17}$$

where the HOT are given by Eq. (A11).The quantities $\bar{\dot{w}}_1$ and $\bar{\dot{w}}_2$, in Eqs. (A14) and (A15), which appear in the temperature form of the energy equation, are related to the rates of production[18] $\dot{w}_i$ through

$$\sum_{i=1}^{N_S}h_i\dot{w}_i = \dot{w}_{sh1}\bar{\dot{w}}_1 + \bar{T}T_{sh}\dot{w}_{sh2}\bar{\dot{w}}_2 \tag{A18}$$

4) Species continuity (nonequilibrium flow), $W = C_i$:

$$\alpha_1 = \frac{1}{\mathrm{PL}_i}\frac{\partial\mathrm{PL}_i}{\partial\eta}\frac{\mathrm{d}g}{\mathrm{d}\bar{\eta}} + \left(\frac{n_{sh}\kappa}{h_1} + \frac{n_{sh}\cos\theta}{h_3}\right) + \frac{n_{sh}n'_{sh}\rho_{sh}u_{sh}\bar{\eta}\bar{\rho}\bar{u}}{\varepsilon^2\mathrm{PL}_ih_1} - \frac{n_{sh}\rho_{sh}}{\varepsilon^2\mathrm{PL}_i}\bar{\rho}v \tag{A19}$$

$$\alpha_2 = -\frac{n^2_{sh}\rho_{sh}\bar{\rho}\dot{w}^1_i}{\varepsilon^2\mathrm{PL}_i} \tag{A20}$$

$$\alpha_3 = \frac{1}{\mathrm{PL}_i}\frac{\partial\mathrm{PM}_i}{\partial\eta}\frac{\mathrm{d}g}{\mathrm{d}\bar{\eta}} + \frac{\mathrm{PM}_i}{\mathrm{PL}_i}\left(\frac{n_{sh}\kappa}{h_1} + \frac{n_{sh}\cos\theta}{h_3}\right) + \frac{n^2_{sh}\rho_{sh}\bar{\rho}\dot{w}^0_i}{\varepsilon^2\mathrm{PL}_i} \tag{A21}$$

$$\alpha_4 = -\frac{n^2_{sh}\rho_{sh}u_{sh}}{\varepsilon^2\mathrm{PL}_ih_1}\bar{\rho}\bar{u} \tag{A22}$$

where

$$\mathrm{PL}_i = \mathrm{PL} = \frac{\mu_{sh}\bar{\mu}}{\mathrm{Pr}}\mathrm{Le} \tag{A23}$$

and

$$\mathrm{PM}_i = \mathrm{PM} = 0 \tag{A24}$$

for binary diffusion.[18]

The quantities $\dot{w}^0_i$ and $\dot{w}^1_i$ appearing in Eqs. (A20) and (A21) are related to the production rates $\dot{w}_i$through the equation

$$\frac{\dot{w}_i}{p} = \dot{w}^0_i - C_i\dot{w}^1_i \tag{A25}$$

References

[1]Williams, R. M., "National Aero-Space Plane: Technology for America's Future," *Aerospace America*, Vol. 24, No. 11, 1986, pp. 18–22.

[2]Lee, K. P., Gupta, R. N., Zoby, E. V., and Moss, J. N., "Hypersonic Viscous Shock-Layer Solutions over Long Slender Bodies—Part II: Low Reynolds Number Flows," *Journal of Spacecraft and Rockets*, Vol. 27, No. 2, 1990, pp. 185–193.

[3]Davis, R. T., "Numerical Solution of the Hypersonic Viscous Shock-Layer Equations," *AIAA Journal*, Vol. 8, No. 5, 1970, pp. 843–851.

[4]Zoby, E. V., Lee, K. P., and Gupta, R. N., "Hypersonic Nonequilibrium Viscous Solutions over Slender Bodies," *Journal of Spacecraft and Rockets*, Vol. 28, No. 3, 1991, pp. 358–360.

[5]Gupta, R. N., and Simmonds, A. L., "Hypersonic Low-Density Solutions of the Navier-Stokes Equations with Chemical Nonequilibrium and Multicomponent Surface Slip," AIAA Paper 86-1349, June 1986.

[6]Gnoffo, P. A., Gupta, R. N., and Shinn, J. L., "Conservation Equations and Physical Models for Hypersonic Air Flows in Thermal and Chemical Nonequilibrium," NASA TP-2867, Feb. 1989.

[7]Anderson, D. A., Tannehill, J. C., and Pletcher, R. H., *Computational Fluid Mechanics and Heat Transfer*, McGraw-Hill, New York, 1984, pp. 417–477.

[8]Probstein, R. F., "Shock-Wave and Flow Field Development in Hypersonic Re-entry," *ARS Journal*, Vol. 31, No. 2, 1961, p. 185.

[9]Gupta, R. N., Lee, K. P., Zoby, E. V., Moss, J. N., and Thompson, R. A., "Hypersonic Viscous Shock-Layer Solutions over Long Slender Bodies—Part I: High Reynolds Number Flows," *Journal of Spacecraft and Rockets*, Vol. 27, No. 2, 1990, pp. 175–184.

[10]Gupta, R. N., Scott, C. D., and Moss, J. N., "Slip-Boundary Equations for Multicomponent Nonequilibrium Air Flows," NASA TP-2452, Nov. 1985; also, *Thermal Design of Aeroassisted Orbital Transfer Vehicles*, edited by H. F. Nelson, Vol. 96, Progress in Astronautics and Aeronautics, AIAA, New York, 1985, pp. 465–490.

[11]Gupta, R. N., and Nayani, S. N., "Low-Density Flow Effects for Hypervelocity Vehicles," Air Force Flight Dynamics Lab., Wright Patterson AFB, OH, WRDC-TR-90-3007, March 1990.

[12]Gupta, R. N., Nayani, S. N., Lee, K. P., and Zoby, E. V., "Higher-Order Viscous Shock-Layer Solutions for High Altitude Flows," AIAA Paper 93-2724, July 1993.

[13]Cheng, H. K., "The Blunt Body Problem in Hypersonic Flow at Low Reynolds Number," Cornell Aeronautical Lab., Rept. AF-1285-A-10, Buffalo, NY, June 1963.

[14]Blottner, F. G., Johnson, H., and Ellis, M., "Chemically Reacting Viscous Flow Program for Multi-Component Gas Mixtures," Sandia Labs., Rept. SC-RR-70-754, Albuquerque, NM, Dec. 1971.

[15]Cheng, H. K., "Viscous Hypersonic Blunt-Body Problems and the Newtonian Theory," *Fundamental Phenomena in Hypersonic Flow*, edited by J. G. Hall, Cornell Univ. Press, Ithaca, NY, 1966, pp. 90–131.

[16]Gupta, R. N., Yos, J. M., Thompson, R. A., and Lee, K. P., "A Review of Reaction Rates and Thermodynamic and Transport Properties for an 11-Species Air Model for Chemical and Thermal Nonequilibrium Calculations to 30000K," NASA TP-1232, Aug. 1990.

[17]Mason, E. A., and Saxena, S. C., "Approximation Formula for the Thermal Conductivity of Gas Mixtures," *Physics of Fluids*, Vol. 1, No. 5, 1958, pp. 361–369.

[18]Lee, K. P., and Gupta, R. N., "Viscous-Shock-Layer Analysis of Hypersonic Flows," NASA CR-189614, March 1992.

[19]Srivastava, B. N., David, R. T., and Werle, M. J., "Slip Model for Hypersonic Viscous Flow," *AIAA Journal*, Vol. 14, No. 2, 1976, pp. 257–259.

[20]Jain, A. C., and Adimurthy, V., "Hypersonic Merged Stagnation Shock Layers, Part I: Adiabatic Wall Case," *AIAA Journal*, Vol. 12, No. 3, 1974, pp. 342–347.

[21]Potter, J. L., and Bailey, A. B., "Pressures in the Stagnation Region of Blunt Bodies in the Viscous Layer to Merged Layer Regimes of Rarefied Flow," Arnold Engineering Development Center, Rept. AEDC-TDR-63-168, Tullahoma, TN, Sept. 1963.

[22]Dogra, V. K., Moss, J. N., and Price, J. M., "Near Wake Structure for a Generic ASTV Configuration," AIAA Paper 93-0271, Jan. 1993.

Space Manufacturing 9

The High Frontier

Accession, Development and Utilization

Barbara Faughnan, editor

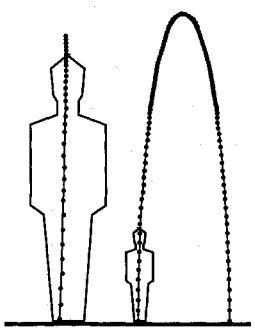

1993, 441 pp, illus, Hardback
ISBN 1-56347-063-2
AIAA Members $59.95
Nonmembers $79.95
Order #: SMF-9(945)

This volume presents the proceedings of the 11th Conference on Space Manufacturing. All major areas of consideration for the development of space-based manufacturing and the movement of humans into productive long-term occupancy of environments off of the Earth's planetary surface are covered. This includes ideas ranging from social sciences through propulsion, materials science and engineering issues. Chapters include: Transportation and Materials; Policy; Social and Medical Sciences; Structures; Space Applications, and more.

You may also order other volumes in the series by calling 1-800/682-AIAA.

Place your order today! Call 1-800/682-AIAA

AIAA
American Institute of Aeronautics and Astronautics

Publications Customer Service, 9 Jay Gould Ct., P.O. Box 753, Waldorf, MD 20604
FAX 301/843-0159 Phone 1-800/682-2422 9 a.m. - 5 p.m. Eastern

Sales Tax: CA residents, 8.25%; DC, 6%. For shipping and handling add $4.75 for 1-4 books (call for rates for higher quantities). Orders under $100.00 must be prepaid. Foreign orders must be prepaid and include a $20.00 postal surcharge. Please allow 4 weeks for delivery. Prices are subject to change without notice. Returns will be accepted within 30 days. Non-U.S. residents are responsible for payment of any taxes required by their government.